



## ORIGINAL RESEARCH PAPER

# Simulation of positive streamer propagation in an air gap with a GFRP composite barrier

Hengxin He<sup>1</sup>  | Dezhi Xia<sup>1</sup> | Bin Luo<sup>1</sup>  | Weijiang Chen<sup>2</sup> | Kai Bian<sup>2</sup> | NianWen Xiang<sup>3</sup>

<sup>1</sup>State Key Laboratory of Advanced Electromagnetic Engineering and Technology, Huazhong University of Science and Technology, Wuhan, China

<sup>2</sup>State Grid Corporation of China, Beijing, China

<sup>3</sup>School of Electrical Engineering and Automation, Hefei University of Technology, Hefei, China

## Correspondence

Bin Luo, State Key Laboratory of Advanced Electromagnetic Engineering and Technology, Huazhong University of Science and Technology, Wuhan 430074, China.  
Email: binluo931@gmail.com

Associate Editor: Yuriy Serdyuk

## Funding information

National Key Laboratory Foundation of China, Grant/Award Number: 2017YFB0902701

## Abstract

The puncture of glass fibre reinforced polymer (GFRP) laminate is a primary damage pattern of wind turbine blades due to lightning strikes. A numerical simulation model of positive streamer propagation in a needle-to-plate air gap with a GFRP laminate is established to investigate the breakdown mechanism of GFRP laminate. The model not only considers the dynamics of charged particles in the air and the composite laminate, but also the current continuity at gas–solid interfaces. The simulated streamer discharge pattern and the surface streamer length are in good agreement with the observation results. The distributions and evolutions of the electron number density, electric field, and surface charge densities during streamer propagation are obtained. It is found that the enhancement of the electric field on the GFRP laminate is caused by the rapid deposition of positive and negative space charges on the GFRP laminate after a secondary streamer incepts on the lower surface of the GFRP laminate. The effects of the applied voltage, relative permittivity, and thickness of the GFRP laminate on the electric field on the GFRP laminate are investigated. The obtained results could assist in further understanding of the mechanism of GFRP wind blade breakdown due to lightning strikes.

## 1 | INTRODUCTION

Wind power is a widely used renewable energy generation technology. Increasingly high demand for wind energy has been contributing to the improvement in capacity per wind turbine by increasing their height. The increase in the heights of wind turbines promotes the possibility of lightning strikes on wind turbine blades, making lightning strikes an increasingly important source of damage to wind turbine blades [1–3]. Wind turbine blades are widely made of glass fibre reinforced polymer (GFRP), with several groups of lightning receptors located close to their tips to prevent the direct attachment of a lightning leader to the blades. Inside a blade, a down conductor is laid to release the return stroke current to the ground, as shown in Figure 1. Field experience shows that more than 90% of lightning damage occurs at the last 4 m of the blade tip, which mainly consists of burns, punctures, and delamination of blade structures [4, 5]. Among these damages, puncture of the GFRP laminate is the most severe, and could lead to blade

fracture when the wind turbine continuously bears mechanical loads during long-term operation.

The thermal effect of the return stroke current is believed to be the cause of puncture damage to wind turbine blades [6, 7]. To investigate lightning thermal damage to wind blades, many researchers have carried out impulse current tests on blades and laminates made of GFRP and carbon fibre reinforced polymer (CFRP) [8]. It was concluded that the maximum ablation depth of the composite layers only reaches the millimetre level under varying transferred charges. The low ablation depth shows that the thermal effect of the lightning current may fail to cause puncture damage to the composite layers [9].

Electric breakdown is another possible reason for puncture damage to wind turbine blades. As the lightning downward leader approaches a wind turbine blade, the enhanced ambient electric field  $E_{am}$  excited by the charge in the leader channel results in a strengthened electric field on the composite layer near the blade tip [10]. When the electric field exceeds the critical breakdown field of the GFRP laminates, the electric breakdown

This is an open access article under the terms of the Creative Commons Attribution License, which permits use, distribution and reproduction in any medium, provided the original work is properly cited.

© 2021 The Authors. *High Voltage* published by John Wiley & Sons Ltd on behalf of The Institution of Engineering and Technology and China Electric Power Research Institute.

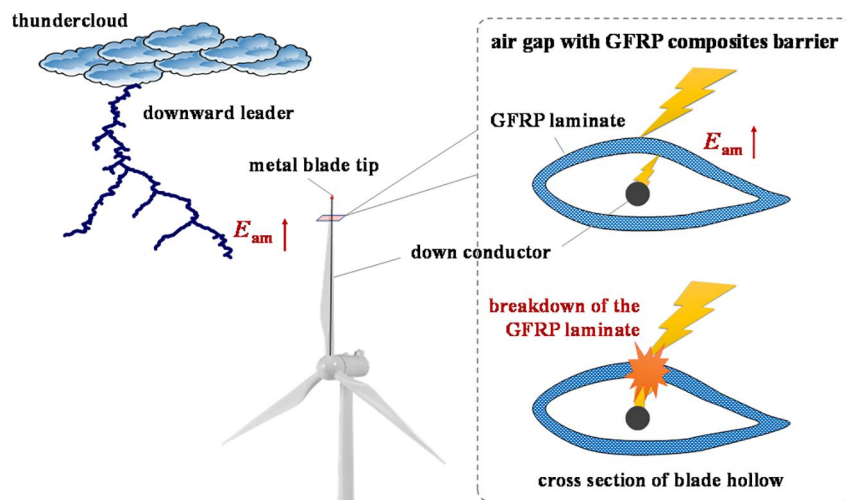


**FIGURE 1** Breakdown of the air-GFRP composite gap during a lightning strike on a wind turbine blade

might lead to the formation of pores on the composite material, leaving a path to bridge the lighting downward leader and the down conductor. The current of the lightning return stroke can heat and expand the breakdown pores in the composite layer, which results in puncture damage to the blade. Discharge experiments in a long air gap have been carried out to investigate the electric breakdown of wind turbine blades during natural lightning strikes [11]. Yokoyama studied the lightning attachment to a 3-m GFRP blade sample [12]. It was observed that the lightning leader could cause electric breakdown of the GFRP laminate with a polluted surface and directly strike the down conductor. In [13], the breakdowns of GFRP laminates were studied in discharge experiments in a 3 m air gap, with residual surface discharges recorded in the vicinity of breakdown channels. In [14], streamer discharge experiments were carried out in a 7 mm rod-plate air gap with a GFRP laminate barrier. Breakdowns of the GFRP laminates were observed with the formation of secondary streamer discharge channels between the GFRP laminates and the grounded plate electrode. Although multiple discharge experiments have been conducted, the correlation of the observed discharge phenomenon to the breakdown of the GFRP laminate was not fully understood. To study the barrier effect of a solid dielectric during discharge breakdown in a rod-plate gap, a fluid dynamic model of streamer discharge in a gas-solid composite gap has been established [15], considering the drift, diffusion, and chemical reactions of charged particles. Although the streamer discharge and surface discharge in the composite gap were discussed, the electric field stressed on the solid dielectric was not presented. Since a strong electric field on the GFRP laminate may be a dominant factor that triggers the breakdown pores, a quantitative analysis of the electric field stressed on the GFRP laminate during streamer discharge in the air-GFRP composite gap is crucial to understanding the mechanism of the formation of the puncture damage on the GFRP blade during a lightning strike.

A numerical simulation model of streamer discharge is established herein, which considers the dynamics of charged particles in the air and GFRP laminate, and the current continuity on gas-solid interfaces. The inception and propagation of a

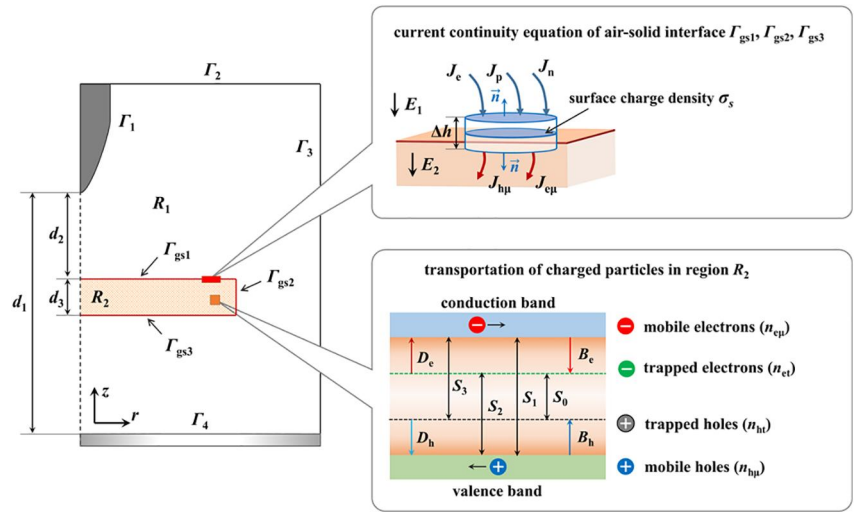
positive streamer in the gas-solid composite gap are simulated and compared with experimental observations. Based on the simulation results, the effect of streamer propagation on surface charge deposition on the GFRP laminate is analysed. The effect of the GFRP laminate thickness on the average electric field stressed on the laminate is discussed, and an electric breakdown mechanism of the GFRP laminate is proposed. The work described here can assist in the study of the breakdown mechanism and protection technology of the GFRP composite laminate of wind turbine blades under lightning strikes.

## 2 | NUMERICAL MODEL OF POSITIVE STREAMER DISCHARGE IN AN AIR-GFRP COMPOSITE GAP

### 2.1 | General description

Electrostatic field analysis shows that the surface electric field of the down conductor near a blade tip can reach the MV/m level when a lightning downward leader approaches the blade [12]. Under this strong electric field, a positive streamer discharge may inception on the surface of the down conductor. Space charge at the positive streamer head may accumulate on the inner surface of the blade, which may strengthen the electric field on the exterior surface of the blade and further trigger the development of the secondary streamer discharge, as shown in Figure 1. The breakdown of the GFRP composite laminate of a wind blade depends on the superposition of the ambient electric field and the space charge field during streamer discharge. Since the space charge generated during streamer discharge may greatly strengthen the total electric field on the GFRP laminate and lead to puncture damage of blades, it is crucial to study positive streamer discharge in the air-GFRP composite gap. Since simulating the streamer branching by kinetic or particle description such as Monte Carlo simulation or Boltzmann transport solution in 3D is challenging and impractical in computational resources and time, a two-dimensional axisymmetric fluid dynamic model of

**FIGURE 2** Illustration of the modelling of streamer discharge in the air–GFRP gap



streamer discharge in the composite gap is established to simulate the development of streamer discharge in a two-dimensional axisymmetric electrode and gap configuration, aimed at obtaining the superposition electric field on the GFRP laminate, as shown in Figure 2.

The model adopts a typical needle–plate gap. A GFRP dielectric plate is horizontally placed in the gap. The length of the needle–plate gap is denoted as  $d_1$ . The needle electrode is hyperbolic with a curvature radius  $r_c$ . The radius of the grounded plate electrode is denoted as  $r_p$ . The thickness and radius of the dielectric plate are denoted as  $d_3$  and  $r_d$ , respectively. The distance between the upper surface of the dielectric plate and the electrode tip is denoted as  $d_2$ . Compared with conventional streamer discharge fluid models in an air gap, the established streamer discharge model in the gas–solid composite gap describes not only the dynamics of charged particles in the air region but also the dynamics of charged particles in the GFRP composite laminate and the current continuity on gas–solid interfaces. Although the charged transport in the poorly conductive GFRP is so slow that it may be negligible during streamer discharge, the CFRP, which is a potential material for wind turbine blades and aircraft, has such a high conductivity that the strengthened charge transport may lead to distinct discharge characteristics observed in experiments [16]. To ensure a relatively comprehensive physical description and improve the applicability of the model in the highly conductive material, the charge transport in the GFRP laminate is reserved. The computational domain of the model is divided into an air region  $R_1$ , GFRP composite laminate region  $R_2$ , and gas–solid interfaces  $\Gamma_{gs1}$ ,  $\Gamma_{gs2}$ , and  $\Gamma_{gs3}$ . The governing equations in each domain are described in Section 2.2.

## 2.2 | Governing equations

In the air region, the drift, diffusion, and chemical reactions of electrons, positive ions, and negative ions are considered. As the applied voltage of the needle electrode exceeds the

streamer onset voltage, the streamer can inception and propagate in the air region  $R_1$ . The continuity equations of the three charged particles are:

$$\frac{\partial n_e}{\partial t} + \nabla \cdot (-n_e \mu_e \mathbf{E} - D_e \nabla n_e) = S_e \quad (1)$$

$$\frac{\partial n_p}{\partial t} + \nabla \cdot (n_p \mu_p \mathbf{E} - D_p \nabla n_p) = S_p \quad (2)$$

$$\frac{\partial n_n}{\partial t} + \nabla \cdot (-n_n \mu_n \mathbf{E} - D_n \nabla n_n) = S_n \quad (3)$$

where  $\mathbf{E}$  is the electric field vector; and  $n_e$ ,  $n_p$ , and  $n_n$  are the number densities of electrons, positive ions, and negative ions, respectively.  $\mu_e$ ,  $\mu_p$ , and  $\mu_n$  are the mobilities of electrons, positive ions, and negative ions, respectively.  $D_e$ ,  $D_p$ , and  $D_n$  are the diffusion coefficients of electrons, positive ions, and negative ions, respectively.  $S_e$ ,  $S_p$ , and  $S_n$  denote the source terms of the electrons, positive ion, and negative ions. The source term  $S_e$  of electrons is expressed as

$$S_e = \alpha n_e \mu_e E - \eta n_e \mu_e E - \beta_{ep} n_e n_p + S_0 + S_{ph} \quad (4)$$

where  $\alpha$  is the collisional ionisation coefficient;  $\eta$  is the electron attachment coefficient considering the contributions of two-body and three-body attachments;  $\beta_{ep}$  is the recombination coefficient of electrons and positive ions;  $S_0$  and  $S_{ph}$  are background ionisation and photoionisation rates, respectively. The photoionisation model recommended by Zheleznyak is used to calculate  $S_{ph}$  [17]. Similarly, the source terms of positive ions and negative ions is expressed as

$$S_p = \alpha n_e \mu_e E - \beta_{ep} n_e n_p - \beta_{np} n_n n_p + S_0 + S_{ph} \quad (5)$$

$$S_n = \eta n_e \mu_e E - \beta_{np} n_n n_p \quad (6)$$

where  $\beta_{np}$  is the recombination coefficient of negative and positive ions. Parameters in the governing equations in the air region under atmospheric pressure are taken from [15].

In the conduction band of the GFRP laminate, there are a few slightly mobile free electrons, whose number density is denoted as  $n_{em}$ . The number density of mobile free holes in the conduction band is denoted as  $n_b$ . Under the applied electric field, the dynamics of free electrons and holes in the conduction band can be described by fluid dynamic equations:

$$\frac{\partial n_{em}}{\partial t} + \nabla \cdot (-n_{em}\mu_{em}\mathbf{E} - D_{em}\nabla n_{em}) = S_{em} \quad (7)$$

$$\frac{\partial n_b}{\partial t} + \nabla \cdot (n_b\mu_b\mathbf{E} - D_b\nabla n_b) = S_b \quad (8)$$

where  $\mu_{em}$  and  $\mu_b$  are the mobilities of free electrons and holes in the conduction band, respectively;  $D_{em}$  and  $D_b$  are the diffusion coefficients of free electrons and holes, respectively;  $S_{em}$  and  $S_b$  are the source terms of free electrons and holes, respectively. As shown in Figure 2, the free electrons in the conduction band can be captured by traps to become trapped electrons. Additionally, trapped electrons can escape deep traps and become free electrons. Similarly, free holes may fall into deep traps to become trapped holes, while trapped holes are likely to jump to the conduction band and become free holes after absorbing proper energy. There are recombination reactions between electrons and holes in the GFRP laminate, which can be described by four recombination coefficients with different subscripts. Denoting the number densities of trapped electrons and trapped holes as  $n_{et}$  and  $n_{ht}$ , respectively, the source terms  $S_{em}$  and  $S_b$  of free electrons and holes are calculated as:

$$S_{em} = -R_{emb}n_{em}n_b - R_{embt}n_{em}n_{bt} - T_{em}n_{em}\left(1 - \frac{n_{et}}{n_{0et}}\right) + vn_{et}\exp\left(\frac{-\psi_{et}}{kT}\right)\frac{n_{et}}{n_{0et}} \quad (9)$$

$$S_b = -R_{emb}n_{em}n_b - R_{bet}n_bn_{et} - T_bn_b\left(1 - \frac{n_{ht}}{n_{0ht}}\right) + vn_{ht}\exp\left(\frac{-\psi_{ht}}{kT}\right)\frac{n_{ht}}{n_{0ht}} \quad (10)$$

where  $n_{0et}$  and  $n_{0ht}$  are the initial densities of trapped electrons and trapped holes, respectively.  $R_{emb}$  is the recombination coefficient of free electrons and free holes.  $R_{embt}$  is the recombination coefficient of free electrons and trapped holes.  $R_{bet}$  is the recombination coefficient of trapped electrons and free holes.  $T_{em}$  and  $T_b$  are the trapping coefficients of free electrons and holes, respectively.  $v$  is the attempt-to-escape frequency; and  $\psi_{et}$  and  $\psi_{ht}$  are barrier energies for de-trapping of the trapped electrons and holes, respectively.  $T$  is the ambient temperature, taken as the room temperature of

300 K.  $k$  is the Boltzmann constant. The drift and diffusion of free electrons and holes in the GFRP laminate are described by the effective mobility coefficient and diffusion coefficient:

$$\mu_{em,b} = \mu_{bem,bh}\exp\left(\frac{-\psi_{sem,sh}}{kT}\right) \quad (11)$$

$$D_{em,b} = \left(\frac{kT}{e}\right)\mu_{em,b} \quad (12)$$

where the subscripts  $em$  and  $b$  represent the free electrons and holes, respectively.  $\mu_{bem}$  and  $\mu_{bh}$  are the band mobilities for free electrons and holes, respectively.  $\psi_{sem}$  and  $\psi_{sh}$  are the depths of electron traps and hole traps, respectively.  $e$  is the elementary charge.

Since the trapped electrons and trapped holes cannot drift under the electric field, the dynamics of  $n_{et}$  and  $n_{ht}$  are described by the following time-variant equations:

$$\frac{\partial n_{et}}{\partial t} = -R_{etb}n_{et}n_b - R_{etbt}n_{et}n_{bt} + T_{em}n_{em}\left(1 - \frac{n_{et}}{n_{0et}}\right) - vn_{et}\exp\left(\frac{-\psi_{et}}{kT}\right)\frac{n_{et}}{n_{0et}} \quad (13)$$

$$\frac{\partial n_{ht}}{\partial t} = -R_{embt}n_{em}n_{ht} - R_{etbt}n_{et}n_{ht} + T_bn_b\left(1 - \frac{n_{ht}}{n_{0ht}}\right) - vn_{ht}\exp\left(\frac{-\psi_{ht}}{kT}\right)\frac{n_{ht}}{n_{0ht}} \quad (14)$$

where  $R_{etbt}$  is the recombination coefficient of trapped electrons and trapped holes. Solving Equations (5)–(14) yields the dynamics of charged particles in the GFRP laminate. Since GFRP is a composite material, the parameters in the charge transport model are difficult to obtain and few parameters have been reported. Discharge experiments of CFRP and GFRP show that the conductivity and relative permittivity are two crucial parameters affecting the discharge characteristics and electric field on the barrier [16]. The alternative way adopted is to adjust the band mobility to ensure a conductivity consistent with the measured one. When the electron and hole band mobilities are adjusted to  $1 \times 10^{-14}$  m<sup>2</sup>/V/s and  $2 \times 10^{-13}$  m<sup>2</sup>/V/s, the simulated steady conductivity is about  $10^{-15}$  S/cm, which is close to the measured conductivity for a GFRP laminate in [16]. The dielectric constant is set as 4.6, which also can be found in [16].

The Schottky mechanism reveals that a fraction of accumulated charge on the gas–solid interfaces can be injected into the solid dielectrics. The injected current density is expressed as:

$$J_{a,c} = AT^2 \exp\left(-\frac{\psi_{a,c}}{kT}\right) \exp\left(e\frac{\sqrt{eE_{a,c}/4\pi\epsilon_0\epsilon_r}}{kT}\right) \quad (15)$$



where the subscript  $a$  represents the anode, which generates a positive charge injection. The subscript  $c$  represents the cathode, which generates a negative charge injection.  $A$  is the Richardson constant having a value of  $1.2 \times 10^6 \text{ A}/(\text{m}^2\text{K}^2)$ .  $\psi_a$  and  $\psi_c$  are the injection barrier energies (eV) of positive and negative charges, respectively.  $\epsilon_0$  is the vacuum permittivity.  $\epsilon_r$  is the relative permittivity of the GFRP laminate. Although Equation (15) was obtained in the case of direct electrode–dielectric contact, this equation is a promising choice to model the current injection process in the streamer–dielectric contact case and has been adopted in [15]. Note that in this case,  $E_a$  and  $E_c$  represent the electric field at the gas–solid interfaces in the air and solid dielectric regions, respectively.

In the gas–solid composite gap, the positive streamer starts from the tip of the needle electrode and propagates towards the GFRP laminate. The positive ions generated by streamer discharge move towards the GFRP laminate and deposit on the top surface  $\Gamma_{gs1}$  to form the positive space charge. A small fraction of the positive ions can be injected into the GFRP laminate and form holes in the laminate through the Schottky mechanism. Owing to the hole injection on the top surface  $\Gamma_{gs1}$ , the reduction in the normal flux of positive ions on  $\Gamma_{gs1}$ ,  $-J_{ip}/e$ , has to be applied as a boundary condition when solving Equation (2) to ensure the conservation of positive ions. Similarly, when Equation (8) is solved, it is necessary to apply hole injection flux  $J_{ip}/e$  on  $\Gamma_{gs1}$  to ensure the accurate treatment of the additional hole source. The injected current  $J_{ip}$  is calculated using Equation (15).

In contrast to the case of positive ions, the electrons generated by streamer discharge in air move towards the GFRP laminate under the electric field, contributing to electron injection on the lower surface  $\Gamma_{gs2}$ . In the same way, the reduction in the normal flux of  $-J_{ie}/e$  is applied on  $\Gamma_{gs2}$  when solving Equation (1), where  $J_{ie}$  is the injected electronic current calculated using Equation (15). When solving Equation (7), the injected flux  $J_{ie}/e$  of free electrons is applied on boundary  $\Gamma_{gs2}$ .

The surface charge density  $\sigma_s$  accumulated on gas–solid interfaces  $\Gamma_{gs1}$ ,  $\Gamma_{gs2}$ , and  $\Gamma_{gs3}$  is calculated using the current continuity equation:

$$-\frac{\partial \sigma_s}{\partial t} = J_{gn} + J_{sn} \quad (16)$$

where  $J_{gn}$  is the normal component of current density in air region  $R_1$ .  $J_{sn}$  is the normal component of current density in the GFRP laminate.  $J_{gn}$  and  $J_{sn}$  are expressed as:

$$J_{gn} = J_e + J_n + J_p = (en_e\mu_e + en_n\mu_n + en_p\mu_p)\mathbf{E}_{air} \cdot \mathbf{n} \quad (17)$$

$$J_{sn} = J_{em} + J_b = (en_{em}\mu_{em} + en_b\mu_b)\mathbf{E}_{solid} \cdot \mathbf{n} \quad (18)$$

where  $J_e$ ,  $J_n$ , and  $J_p$  are the outward normal current densities of electrons, positive ions, and negative ions in the air region at

the interface.  $J_{em}$  and  $J_b$  represent the outward normal current densities of free electrons and holes in the GFRP region at the interface.  $\mathbf{E}_{air}$  is the electric field vector in the air region at the interface.  $\mathbf{E}_{solid}$  is the electric field vector in the solid dielectric region at the interface.  $\mathbf{n}$  refers to the outward normal vector at the interface, as shown in Figure 2. Note that increases in the current density  $J_{gn}$  in the air region  $R_1$  and the current density  $J_{sn}$  in the GFRP laminate region  $R_2$  decrease the surface charge density.

To accurately simulate streamer discharge, the distortion effect of space charge and surface charge on the ambient field should be considered. In the model described here, Poisson Equations (19) and (20) are used to describe the impact of the distortion of space charge on the electric field in air and GFRP laminate domains, respectively. The surface charge is considered as a boundary condition in Equation (21) to account for the jump of the electric field at the interfaces. Equations (19)–(21) are presented as:

$$\nabla \cdot (\epsilon_0 \mathbf{E}_g) = e(n_p - n_e - n_n) \quad (19)$$

$$\nabla \cdot (\epsilon_0 \epsilon_r \mathbf{E}_s) = e(n_b + n_{ht} - n_{em} - n_{et}) \quad (20)$$

$$\mathbf{e}_n \cdot (\epsilon_0 \epsilon_r \mathbf{E}_s - \epsilon_0 \mathbf{E}_g) = \sigma_s \quad (21)$$

where  $\mathbf{E}_g$  and  $\mathbf{E}_s$  represent the spatial electric fields in the air and GFRP domains, respectively. The right side of Equation (19) represents the space charge density in the air region  $R_1$ , which is determined by the number densities of the three charged particles ( $n_e$ ,  $n_n$ , and  $n_p$ ) generated by streamer discharge. The right side of Equation (20) represents the space charge density in the GFRP laminate region  $R_2$ , which is determined by the number densities of the four charged particles ( $n_{em}$ ,  $n_b$ ,  $n_{ht}$ , and  $n_{et}$ ) in the laminate. The right side of Equation (21) stands for the surface charge surface density  $\sigma_s$  on gas–solid interfaces.  $\mathbf{e}_n$  is the unit vector at the gas–solid interface, which points from the air region to the solid dielectric region.

The streamer discharge in the gas–solid composite gap is characterised by a strong gradient of the electric field at the streamer head, strong coupling of the dynamics of the charged particle, and distortion of space electric field, which make an accurate simulation difficult to achieve. Therefore, it is necessary to adopt appropriate mesh and solver settings, which could not only capture the sharp variation in the electric field at the streamer head but also accurately solve the tightly coupling multiple physical fields. The axial mesh resolution between the needle electrode and GFRP laminate is set as 1/1600 cm to resolve the electric field at the streamer head with the largest gradient near the needle electrode. The axial mesh resolution between the bottom of the GFRP laminate and the grounded plate electrode is reduced to 1/1000 cm, whereas the mesh resolution at the surfaces of the GFRP laminate is 1/1200 cm. The simulated electric fields show that the adopted mesh

accurately captures rapid and sharp changes in the electric field at the streamer head and ensures the reliability of simulation results.

The separation solver is used to solve the coupling model of streamer discharge, with governing equations of charged species in the air region and the Poisson equation, governing equations of charged species in the GFRP region, and Helmholtz equations of photoionisation in three different separation steps, respectively. The implementation of separation solvers improves the convergence and accuracy of simulation results and reduces the computational resource. The finite element method with an unstructured mesh is used to spatially discretise all the equations. To suppress the numerical diffusion and oscillation of Equation (1) solved by the finite element method, the streamline diffusion method is adopted for stabilisation. The backward difference method is used for time stepping. The maximum time step is set as 0.01 ns to reduce error accumulation. The smooth electric field and surface charge distributions indicate that the numerical oscillation and time-stepping error can be reduced, ensuring the accuracy of simulation results.

### 3 | MODEL VALIDATION

To verify the accuracy of the simulation model, the streamer discharges in the composite gap in [16] are simulated and compared with the experimental observations. In [16], the gap length between the needle and plate is 7.4 mm. The placed GFRP laminate has a thickness of 0.4 mm and a radius of 30 mm. The GFRP laminate is 2 mm from the needle electrode and 5 mm from the grounded plate electrode. The experiment configuration is shown in Figure 3a, where the needle electrode and plate electrode are outlined by a yellow dashed line and a yellow solid line, respectively. A positive square-wave pulse voltage with a rise time of 60 ns is applied to the needle electrode. The recorded image of streamer discharge in Figure 3b shows a surface discharge along the upper surface of the GFRP laminate. Multiple streamer channels are observed between the bottom of the GFRP laminate and the grounded plate electrode. The lengths of surface discharge on the upper surface of the GFRP laminate recorded by the image-intensified charge-coupled device camera (ICCD) are 15.4, 17.5, and 26 mm when the applied voltage amplitudes  $U_{app}$  are 35, 40, and 50 kV, respectively.

The streamer discharges in the composite gap under the same voltages are simulated by the established simulation model in Section 2. Figure 3c shows distributions of the electron number density and electric field at  $t = 20$  ns with an applied voltage amplitude of 40 kV. The electron number density is presented in the logarithm form of  $\log_{10}(n_e)$ , where the unit of  $n_e$  is  $\text{cm}^{-3}$ . The simulation results show that a surface streamer propagates along the upper surface of the laminate, with secondary streamer channels forming between the laminate and grounded plate electrode. The simulated secondary streamer channels shown in Figure 3c may be a reason for the observed streamer branching under the laminate in the experiment. To further verify the accuracy of the

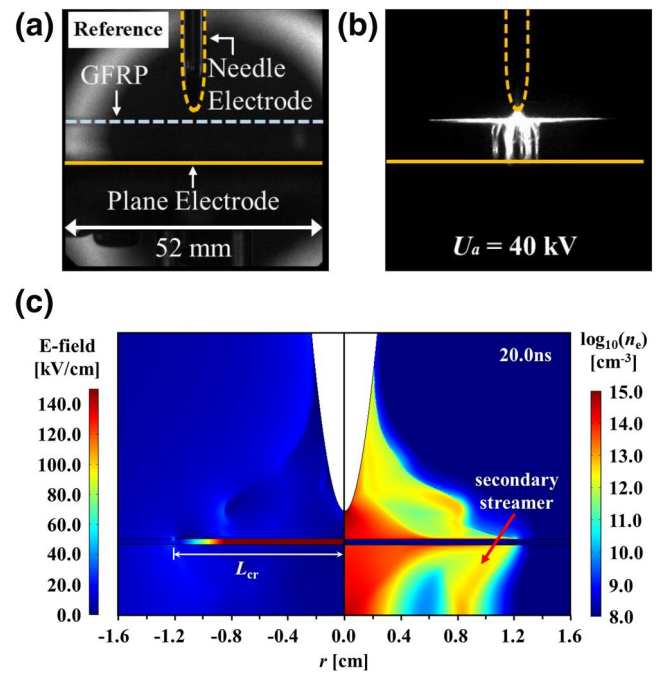


**FIGURE 3** Simulation and experimentally observed streamer discharge patterns in the air–GFRP composite gap: (a) experimental configuration, (b) experimental results, and (c) simulation results. Figures 3 (a) and (b) were reproduced from [16] with permission

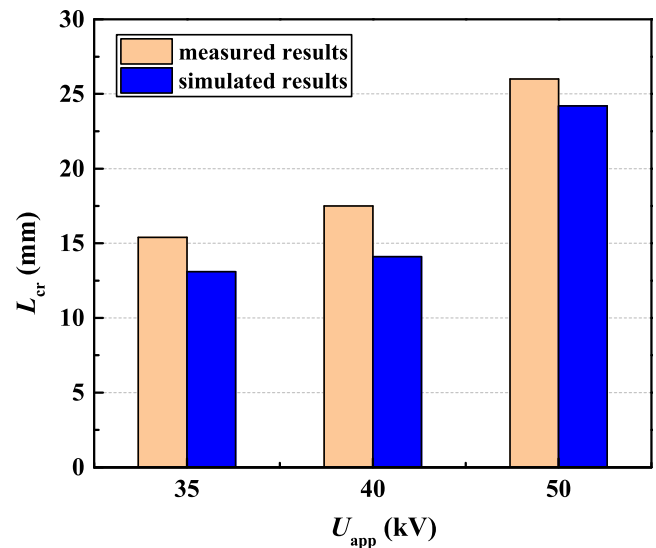


**FIGURE 4** Comparison of simulation and experimental results of the surface streamer length

established model quantitatively, Figure 4 compares the simulated and experimentally observed propagation length  $L_{cr}$  of the surface streamer on the upper surface of the laminate under the same applied voltage conditions. In the simulation, the length of the surface streamer on the top of the barrier is defined as the distance from the streamer head (the position of the maximal electric field) to the axis of symmetry. As the simulated surface discharge propagates so slowly along the top

surface, it does not stop propagating when the simulation stops. However, it can be observed that the velocity of the streamer on the top surface decreases dramatically and its length tends to saturate with time. Hence, an exponential fitting is used to fit the simulation data and determine the maximal propagation length  $L_{cr}$ . Although the propagation lengths  $L_{cr}$  obtained by simulations are slightly shorter than those observed in experiments under the same conditions, the average deviation between the experimental and simulation results under the three conditions is 13.3%. The tolerable small deviation shows the feasibility of the simulation analysis of streamer discharge by using the established model in the gas-solid composite gap.

## 4 | SIMULATION RESULTS

To study the breakdown mechanism of the GFRP laminate in the composite gap, the composite gap structure in [16] is used in this section, with the thickness of the GFRP plate taken as 0.4 mm. The streamer discharge propagation in the composite gap is simulated to analyse the effect of the streamer propagation pattern on the surface charge and electric field strength on the GFRP laminate.

### 4.1 | Streamer discharge patterns

Figure 5 shows variations in the electron number density distribution when the amplitude of the applied voltage on the needle electrode is 50 kV. At  $t = 0.1$  ns, the streamer discharge incepts at the tip of the needle electrode, and the maximal electron number density exceeds  $10^{15} \text{ cm}^{-3}$ . At  $t = 0.2$  ns, the streamer head reaches the upper surface of the GFRP laminate. On the one hand, the concentration region of the electron density develops along the  $r$  direction on the upper surface of

the laminate. On the other hand, owing to the deposition of positive ions on the upper surface of the laminate, the electric field and electron density near the lower surface of the laminate are enhanced. At  $t = 0.3$  ns, the electron density doubles. At  $t > 0.3$  ns, a secondary streamer discharge incepts on the lower surface of the GFRP laminate and propagates towards the grounded plate electrode. Meanwhile, the surface streamer on the upper surface of the GFRP laminate develops along the  $r$  direction. At  $t = 1.0$  ns, the secondary streamer head under the GFRP laminate reaches the grounded plates, resulting in the breakdown of the composite gap.

Figure 6 shows the electric field distribution during the breakdown of the composite gap. As the streamer discharge incepts at the needle electrode, the electric field strengthens at the streamer head. At  $t = 0.2$  ns, the streamer reaches the upper surface of the GFRP laminate, and a strong electric field region at the streamer head then develops along the  $r$  direction. After the inception of the secondary streamer on the lower surface of the laminate, the enhanced field region moves towards the grounded plate electrode. Meanwhile, the axial electric field on the GFRP laminate strengthens. It is shown that the electric field on the GFRP laminate is closely related to the streamer discharge patterns. Therefore, it is important to quantitatively analyse the correlation of the axial average electric field on the GFRP laminate to streamer discharge patterns.

### 4.2 | Average electric field on GFRP

The simulation results presented in Figure 6 show that the axial electric field is strongest after the breakdown of the composite gap. Therefore, this section focuses on the axial field of the GFRP laminate in different streamer discharge stages, for the sake of quantitatively studying the reasons for the laminate breakdown. Since the axial electric field inside GFRP is relatively uniform due to its low conductivity and current injection,

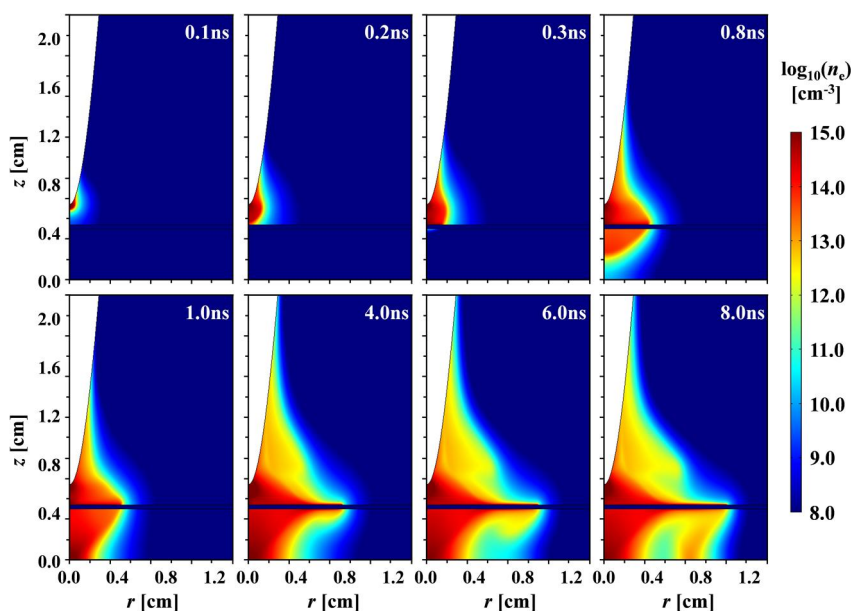
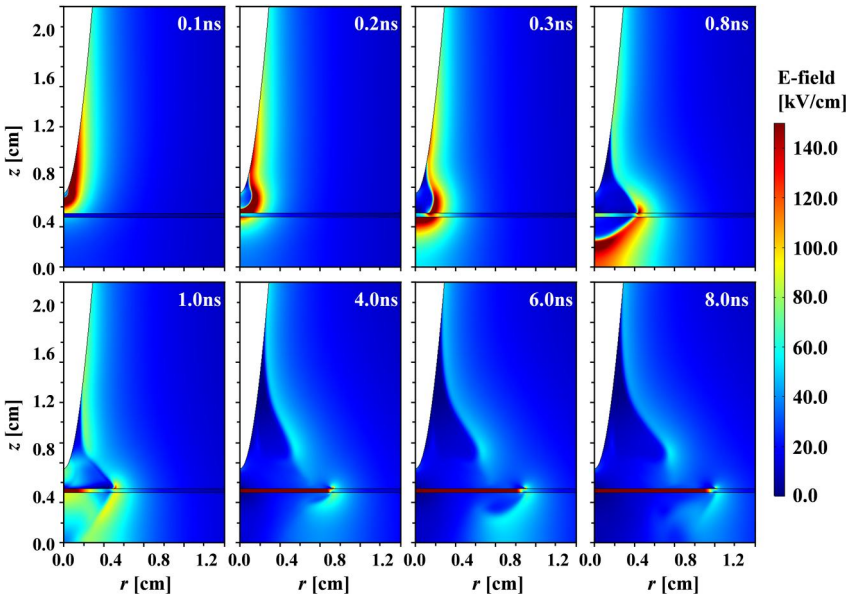
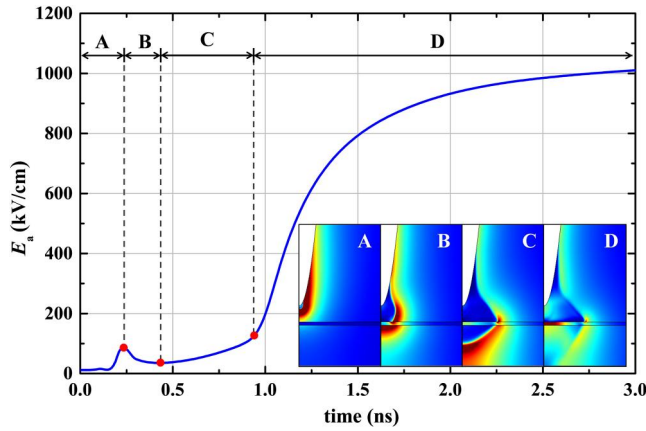


FIGURE 5 Distribution of the electron density during streamer discharge in the composite gap



**FIGURE 6** Distribution of the electric field during streamer discharge in the composite gap



**FIGURE 7** Axial average electric field on the GFRP laminate

the main focus here is on the axial average electric field  $E_a$  of the GFRP laminate, which is defined as the ratio of the voltage drop  $\Delta U_g$  on the GFRP laminate to the laminate thickness  $d_3$ . The voltage drop  $\Delta U_g$  can be obtained by integrating the  $z$ -direction components of the electric field in the GFRP laminate at different times.

Figure 7 shows the evolution of  $E_a$  with time, which can be divided into four stages: A, B, C, and D. In stage A, the streamer propagates from the tip of the needle electrode towards the GFRP dielectric plate. The space charge at the streamer head strengthens the electric field in front, resulting in a gradual strengthening of the electric field  $E_a$  on the GFRP laminate. The simulation results show that at  $t = 0.23$  ns, when the streamer head reaches the upper surface of the laminate,  $E_a$  arrives at its first peak value of 86.7 kV/cm. In stage B, the streamer head propagates along the upper surface of the laminate, indicating that the streamer from the needle electrode tip transits into a surface streamer. With the propagation of the

surface streamer, the strengthened electric field region at the surface streamer head moves away from the axis. Although the positive ions generated by streamer discharge gradually deposit on the upper surface of the laminate, the streamer discharge under the laminate has not yet incepted. With the propagation of the surface streamer along the  $r$  direction, the average electric field on the GFRP laminate weakens. At  $t = 0.43$  ns,  $E_a$  reaches its minimal value of 35.2 kV/cm.

In stage C, the secondary streamer incepted under the GFRP laminate and propagates to the grounded plate, with a continuous rise of  $E_a$ . With the inception of the secondary streamer under the laminate, electrons and negative ions drift towards the lower surface of the laminate under the electric field. Except for a fraction of electrons injected into the laminate, most electrons deposit on the lower surface of the laminate and form negative surface charges. The accumulation of positive and negative charges on the surfaces of the laminate increases  $E_a$  continuously. When  $t \geq 0.91$  ns, which is defined as stage D, the streamer under the GFRP laminate reaches the grounded electrode plate, resulting in  $E_a$  increasing more rapidly and then tending to saturate. At  $t = 3.0$  ns, the average electric field  $E_a$  of the laminate strengthens to about 1000 kV/cm, which is 11.6 times that when the streamer from the needle electrode tip just reaches the upper surface of the GFRP laminate. The rapid strengthening of the electric field strength  $E_a$  due to the accumulation of the space charge and surface charge in stage D may cause breakdown of the GFRP laminate during the streamer discharge. The variation in  $E_a$  is related to the sign and density of surface charge deposited on the GFRP laminate during streamer discharge.

### 4.3 | Surface charge density

To explain the variation in the electric field on the GFRP laminate in the combined gap, it is necessary to analyse the



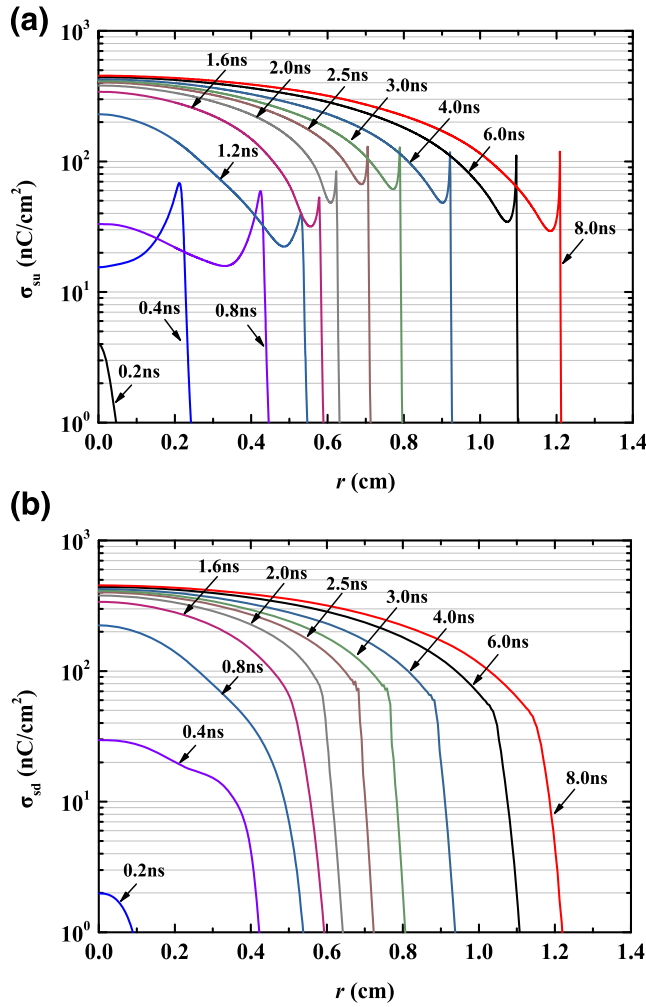


**FIGURE 8** Radial distributions and variations of the absolute values of surface charge densities (a)  $\sigma_{su}$  and (b)  $\sigma_{sd}$  on the GFRP laminate

surface charge densities  $\sigma_{su}$  and  $\sigma_{sd}$  on the upper and lower surfaces of the laminate. The radial distributions of  $\sigma_{su}$  and  $\sigma_{sd}$  during streamer discharge are shown in Figure 8. Figure 8b shows the absolute value of the negative surface charge on the lower surface of the laminate. The surface charge density is referred to as the free surface charge density, which forms due to the current flow difference at the two sides of the interfaces, as described in current continuity Equation (16). At  $t = 0.2$  ns when the streamer head reaches the upper surface of the GFRP laminate, the positive charge density  $\sigma_{su}$  at the upper surface of the laminate has a bell shape of a Gaussian distribution with a maximal value of  $3.0 \text{ nC/cm}^2$  at the axis. During the period from  $t = 0.4$  ns to  $t = 0.8$  ns, the surface streamer on the upper surface of the laminate develops along the  $r$  direction away from the axis. The surface charge density peaks at the surface streamer head. Although the peak value of  $\sigma_{su}$  at the upper surface streamer head decreases,  $\sigma_{su}$  at  $r = 0$  increases with the propagation of the surface streamer. The increase in the axial surface charge  $\sigma_{su}$  may explain the gradual strengthening of the electric field  $E_a$  on the GFRP laminate in stage C. When  $t \geq 0.8$  ns, the position of the peak of  $\sigma_{su}$  shifts

from the surface streamer head to  $r = 0$ . During the period from 1.2 to 2.0 ns, the value of  $\sigma_{su}$  at  $r = 0$  rapidly increases to about  $400 \text{ nC/cm}^2$ , resulting in the rapid increase in strength of the average field on the GFRP laminate in stage D shown in Figure 7. When  $t > 2.0$  ns, the axial surface charge amplitude on the upper surface of the laminate tends to saturate at about  $400 \text{ nC/cm}^2$ .

The negative charges on the lower surface of the GFRP laminate also greatly contribute to the increase in the average electric field of the GFRP laminate. When  $t \geq 0.4$  ns, the streamer incepting on the lower surface of the GFRP laminate propagates towards the grounded plate electrode. The generated electrons are blocked by the GFRP laminate, and negative surface charges thus deposit on the lower surface of the laminate. The absolute value of charge density  $\sigma_{sd}$  increases rapidly with the propagation of the upper surface streamer, as shown in Figure 8b. There is no region of charge concentration moving away from the axis along the radial direction on the lower surface, which indicates that there is no negative surface streamer along the lower surface. This is different from the propagation of the positive streamer along the upper surface of the laminate. During the period from 0.4 to 2.0 ns, the absolute value of the negative surface charge density at  $r = 0$  rises rapidly to the same order as  $\sigma_{su}$ . The synchronous increases in surface charge densities  $\sigma_{su}$  and  $\sigma_{sd}$  at the axis are the main reason for the continuous increase in  $E_a$  in stage C.

## 5 | FACTORS AFFECTING THE ELECTRIC FIELD ON GFRP

This chapter analyzes factors affecting the breakdown of the GFRP laminate based on the variation in the electric field on the GFRP laminate in different streamer discharge stages.

### 5.1 | Applied voltage amplitude

The applied voltage amplitude of the needle electrode varies in the range of 40–70 kV, while the other calculation conditions are consistent with those in Section 4. The simulated electric fields on the GFRP laminate under different voltage amplitudes are shown in Figure 9. Under a certain applied voltage, the variation in the axial average electric field on the GFRP laminate is similar to that in Figure 7. When the voltage applied to the needle electrode increases, the propagation speed of the streamer in the air increases, reducing the duration of stages C and D in Figure 9. The rising time of the axial electric field on the GFRP laminate shortens and the amplitude of the axial electric field rises.

The breakdown electric field  $E_b$  (V/m) of the GFRP laminate with different thicknesses has been obtained in experiments [18] and is expressed as

$$E_b = C_1 \cdot \frac{1}{d} + C_2 \cdot TI \quad (22)$$

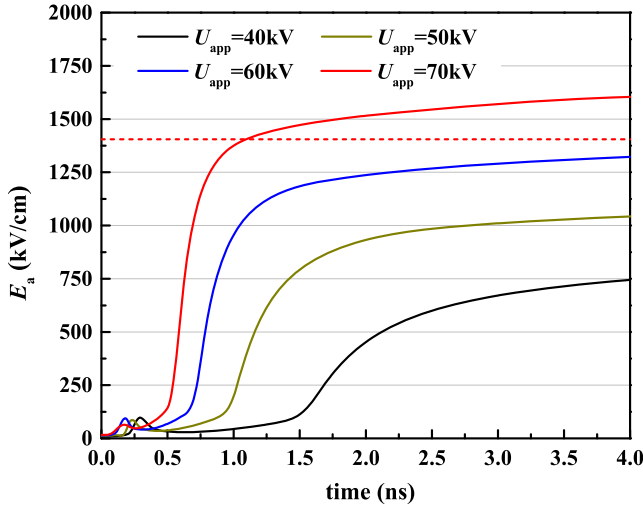


FIGURE 9 Average electric field  $E_a$  on the GFRP laminate under different applied voltages

where  $d$  is the thickness of the GFRP laminate (m);  $TI$  is the leakage tracking index;  $C_1$  and  $C_2$  are constants.  $C_2 \cdot TI$  is taken as a constant equal to  $8 \times 10^6$  and  $C_1$  is equal to  $5.3 \times 10^4$  [10]. The critical average breakdown field strength is 1.41 MV/cm when  $d$  is 0.4 mm. The simulation results in Figure 9 show that only when the voltage amplitude of the needle electrode exceeds 70 kV, does the GFRP laminate break down about 1.1 ns after the streamer inception at the needle electrode tip. In the experiments reported in [16], even though the discharge reaches the plate electrode across the barrier under 40 kV, the GFRP laminate does not suffer electric breakdown due to low electric field on the GFRP laminate, which indicates the failure of the transition from streamer discharge to spark discharge. In fact, the breakdown phenomenon of the GFRP laminate is not observed when the applied voltage reaches 50 kV. This experimental phenomenon is consistent with the simulation prediction that there is no breakdown of the GFRP laminate when the applied voltage is lower than the critical breakdown field strength of 70 kV.

## 5.2 | Relative permittivity of GFRP

Figure 10 shows the variation in the axial average electric field  $E_a$  on the GFRP laminate when  $\epsilon_r$  is equal to 2.3, 4.6, and 6.9, for analysis of the effect of the relative permittivity on the breakdown of the GFRP laminate. The thickness of the laminate  $d_3$  and the applied voltage  $U_{app}$  are fixed at 0.4 mm and 70 kV, respectively. The simulation results show that the variation in permittivity has no appreciable effect on streamer inception. When  $t \geq 0.49$  ns, secondary streamers incept and propagate. In this stage, the variations in the axial average electric field  $E_a$  on the GFRP laminate are consistent under different relative permittivities. The critical average breakdown field strength  $E_b$  on the GFRP laminate is shown as a dotted line in Figure 10. Short time intervals between the intersections of  $E_a$  and  $E_b$  under

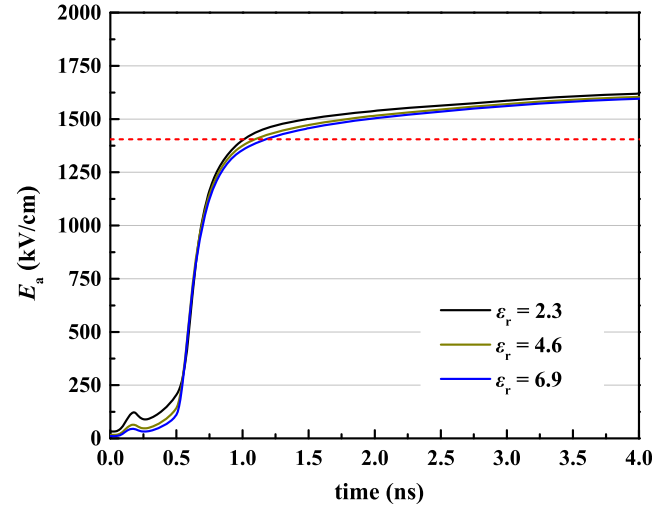


FIGURE 10 Average electric field  $E_a$  on the GFRP laminates with different permittivities

different relative permittivities suggest that the effect of the relative permittivity of the GFRP laminate on the breakdown voltage of the combined gap can be neglected.

To explain why the permittivity has no appreciable effect on the axial average electric field on the GFRP laminate, the distributions of charge density  $\sigma_{su}$  on the upper surface and charge density  $\sigma_{sd}$  on the lower surface of the GFRP laminate for three values of permittivity when  $t = 8.0$  ns are shown in Figure 11. At this time, the streamer has propagated through the combined gap and the axial average electric field  $E_a$  tends to saturate. Figure 11 shows that the increase in  $\epsilon_r$  contributes to a shorter propagation length of the surface streamer and higher concentrated charge densities  $\sigma_{su}$  and  $\sigma_{sd}$  on the upper surface of the laminate at  $t = 8.0$  ns. These phenomena indicate that an increase in  $\epsilon_r$  results in more difficult propagation of the upper surface streamer and easier accumulation of the surface charge densities at the axis. Denoting the normal component of the electric field at  $r = 0$  in the air region as  $E_{1n}$ , as shown in Figure 2, the electric field at  $r = 0$  in the GFRP laminate region  $E_{2n}$  can be obtained using Gauss's law as:

$$E_{2n} = \frac{\sigma_{su} + \epsilon_0 E_{1n}}{\epsilon_0 \epsilon_r} \quad (23)$$

where  $\epsilon_0$  is the vacuum permittivity. After the secondary streamer penetrates the composite gap,  $E_{1n}$  is maintained in a small range of 5–10 kV/cm. The surface charge density  $\sigma_{su}$  on the laminate increases with  $\epsilon_r$ . According to Equation (23), if the ratio of  $\sigma_{su}$  and  $\epsilon_r$  is approximately constant, the electric field  $E_{2n}$  on the GFRP laminate can be assumed to be approximately unchanged. Similarly, Equation (23) is satisfied on the interface between the lower surface on the GFRP laminate and the air, indicating that the ratio of  $\sigma_{sd}$  and  $\epsilon_r$  on the lower surface of the laminate can also be assumed to be unchanged. Hence, an increase in the relative permittivity of the GFRP laminate does not appreciably affect the axial

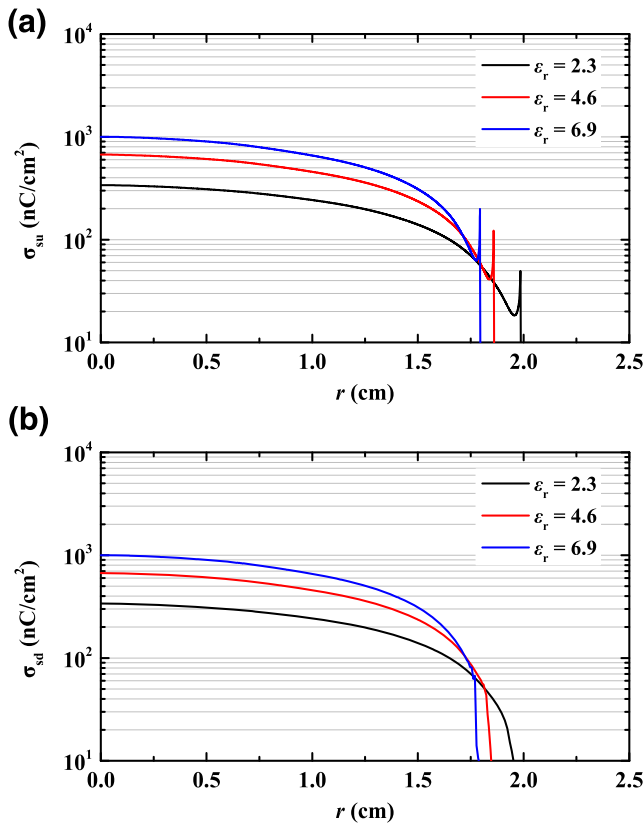


**FIGURE 11** Surface charge densities on the GFRP laminates with different permittivities at  $t = 8.0$  ns

average electric field on the GFRP laminate and the breakdown voltage of the composite gap, although it may increase the axial surface charge density and decrease the surface streamer length along the upper surface.

### 5.3 | Thickness of GFRP

The thickness of the GFRP laminate of actual wind turbine blades gradually increases from the blade tip to the blade root. The thickness  $d_3$  of the GFRP laminate at the blade tip is about 1.0–20.0 mm, while the thickness  $d_3$  at the blade root is about 10 cm. The actual operations of wind turbines show that the breakdown of GFRP laminate mostly occurs at the blade tip. Therefore, it is necessary to analyse the effect of the GFRP laminate thickness on the average electric field  $E_a$  on the GFRP laminate. In this section, the configuration of the composite gap remains unchanged and the applied voltage amplitude remains at 70 kV. Figure 12 shows the variations in the simulated average electric field  $E_a$  on the GFRP laminate when the thickness  $d_3$  is 0.4, 0.8, 1.2, and 2.0 mm, respectively.

The simulation results show that with an increase in thickness  $d_3$ , the average electric field  $E_a$  on the GFRP laminate gradually decreases after the streamer penetrates the composite gap. The onset time of the secondary streamer under the lower surface of the GFRP laminate is more delayed,

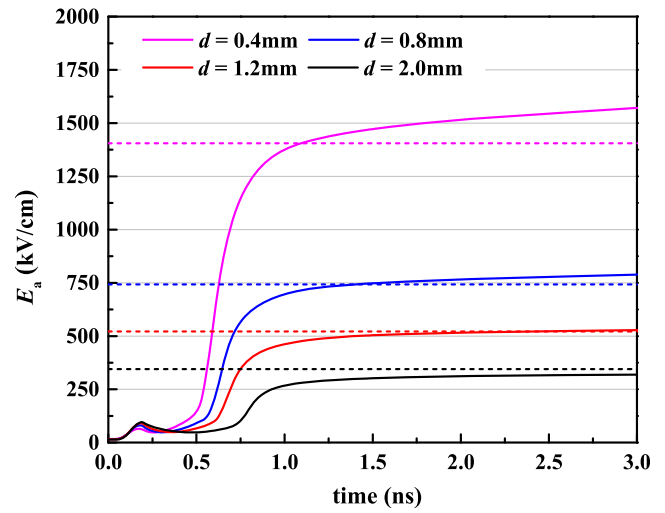


**FIGURE 12** Average electric field  $E_a$  on GFRP laminates with different thicknesses

with an increase in the laminate thickness  $d_3$ . When  $d_3 = 0.4$  mm, the onset time  $t_d$  of the secondary streamer under the lower surface is 0.26 ns. When  $d_3$  increases to 2.0 mm, the onset time of the secondary streamer under the lower surface is delayed to 0.46 ns. Under four different GFRP laminate thicknesses in increasing order, the times at which the secondary streamer head reaches the grounded plate electrode are 0.49, 0.55, 0.62, and 0.74 ns. The average propagation velocities of the corresponding secondary streamers are  $2.2 \times 10^7$ ,  $2.08 \times 10^7$ ,  $1.92 \times 10^7$ , and  $1.79 \times 10^7$  m/s, respectively. An increase in the GFRP laminate thickness reduces the propagation velocity of the secondary streamer. The accumulation speed and amplitude of surface charges on both sides of the GFRP laminate decrease with an increase in the GFRP laminate thickness, which indicates that the amplitude of the axial average electric field on the GFRP laminate decreases.

The dashed lines in Figure 12 show the critical average breakdown field strengths  $E_b$  of GFRP laminates of different thicknesses. When the laminate thickness is 0.4 mm, the average electric field on the GFRP laminate exceeds the critical breakdown field strength of 1.41 MV/cm at  $t = 1.09$  ns, resulting in the breakdown of the GFRP laminate. With an increase in laminate thickness, the breakdown time of the GFRP laminate is gradually delayed when the applied voltage is 70 kV. When  $d_3 = 2.0$  mm, the electric field on the GFRP laminate is weaker than the corresponding critical breakdown electric field, which indicates that the GFRP laminate cannot break down.

In the event of an actual lightning strike on a wind turbine blade, the strong ambient field near the down conductor may contribute to the inception of streamer discharge inside the GFRP blade. The positive space charge generated by the streamer discharge can deposit on the inner surface of the blade, strengthening the electric field on the exterior surface of the blade and thus triggering a secondary streamer discharge. Since the length of the secondary streamer on the exterior

surface of the GFRP blade may reach the order of a metre, the positive surface charge density on the inner surface and the negative surface charge density on the exterior surface of the GFRP blade may reach high magnitudes. The blade tip with a small GFRP blade thickness can bear a stronger average electric field than the blade root with a large thickness. Hence, the blade tip is easier to break down than the blade root. In future work, it will be necessary to carry out experimental observations and numerical simulations on the discharge breakdown of actual wind turbine blades, in order to analyse the effect of the secondary streamer incepting on the exterior surface of the GFRP blade on the puncture damage to the blade quantitatively.

## 6 | CONCLUSIONS

Numerical modelling and simulation analysis of positive streamer propagation in the air–GFRP composite gap were carried out in the present work. Simulation results were compared with experimental observations. The main contributions and conclusions herein are as follows.

- (1) Considering the dynamics of charged particles in the air and GFRP laminate, the current continuity at gas–solid interfaces, and charge injection via the Schottky mechanism at the interfaces, a numerical simulation model of positive streamer propagation in the composite gap was established. The streamer propagation pattern in the composite gap and the length of the surface streamer on the upper surface of the GFRP laminate were obtained, which show good agreement with experimental results.
- (2) The distributions and evolutions of the electron density, electric field, and surface charges on the surfaces of the GFRP laminate were obtained. The inception and propagation of secondary streamers under the GFRP laminate were explained. Analysis of the correlation of the average electric field  $E_a$  on the GFRP laminate to the streamer propagation pattern revealed that the significantly enhanced accumulations of positive surface charge on the upper surface and negative surface charge on the lower surface of the GFRP laminate after the secondary streamer penetrates the gap are the main reasons for the rapid strengthening of the average electric field  $E_a$  on the GFRP laminate.
- (3) With an increase in the applied voltage, the time delay between the secondary streamer inception and its arrival at the grounded plate electrode shortens and the electric field on the GFRP laminate strengthens. The electric field on the GFRP laminate may exceed its critical breakdown field strength, resulting in breakdown of the GFRP laminate. An increase in the relative permittivity of the GFRP laminate may increase the axial surface charge density and reduce the streamer length along the upper surface of the laminate, but it may not have an appreciable effect on the average electric field on the GFRP laminate and breakdown voltage of the composite gap.
- (4) With an increase in GFRP laminate thickness, the propagation velocity of the secondary streamer under the lower surface of the laminate decreases, and the accumulation speed and amplitude of surface charges on both sides of the laminate decrease. Decreases in the accumulation speed and amplitude of the surface charges weaken the axial average electric field on the GFRP laminate. It is thus inferred that the blade tip with a small GFRP blade thickness bears a stronger electric field than the blade root. Hence, the breakdown of the blade tip may be easier. In the future, it will be necessary to carry out experimental observations and numerical simulations on the discharge breakdown of actual wind turbine blades, in order to further quantitatively analyse the effect of a secondary streamer incepting on the exterior surface of the GFRP blade on puncture damage to the blade.

## ACKNOWLEDGEMENT

This work was supported by the National Key Research and Development Program of China (2017YFB0902701).

## ORCID

Hengxin He  <https://orcid.org/0000-0002-1234-5757>

Bin Luo  <https://orcid.org/0000-0003-2419-8683>

## REFERENCES

1. Zeng, R., et al.: Survey of recent progress on lightning and lightning protection research. *High Volt.* 1(1), 2–10 (2016)
2. International Electrotechnical Commission: IEC 61400-24 wind turbines Part 24: lightning protection. IEC (2010)
3. Zhou, Q., et al.: Numerical analysis of lightning attachment to wind turbine blade. *Renew. Energy.* 116, 584–593 (2018)
4. Garolera, A.C., et al.: Lightning damage to wind turbine blades from wind farms in the US. *IEEE Trans. Power Deliv.* 31(3), 1043–1049 (2014)
5. Yasuda, Y., et al.: Classification of lightning damage to wind turbine blades. *IEEE Trans. Electr. Electron. Eng.* 7(6), 559–566 (2012)
6. Chen, W., et al.: Review of research progress in lightning damage and protection of wind turbine blades. *High Volt. Eng.* 45(9), 2782–2796 (2019). (in Chinese)
7. Wang, Y.: Multiphysics analysis of lightning strike damage in laminated carbon/glass fibre reinforced polymer matrix composite materials: a review of problem formulation and computational modelling. *Compos. Appl. Sci. Manuf.* 101, 543–553 (2017)
8. Hirano, Y., et al.: Artificial lightning testing on graphite/epoxy composite laminate. *Compos. Appl. Sci. Manuf.* 41(10), 1461–1470 (2010)
9. Wang, Y., Zhupanska, O.I.: Lightning strike thermal damage model for glass fibre reinforced polymer matrix composites and its application to wind turbine blades. *Compos. Struct.* 132, 1182–1191 (2015)
10. Wang, Y., Zhupanska, O.I.: Estimation of the electric fields and dielectric breakdown in non-conductive wind turbine blades subjected to a lightning stepped leader. *Wind Energy.* 20(5), 927–942 (2017)
11. Gürlek, A.: Breakdown process on rod-rod air gap under oscillating lightning impulse voltage. *High Volt.* 5(3), 319–326 (2020)
12. Yokoyama, S.: Lightning protection of wind turbine blades. *Electr. Power Syst. Res.* 94, 3–9 (2013)
13. Guo, Z., et al.: The performance of lightning protection system of wind turbine blade—a preliminary experimental study. *IEEE Asia-Pacific International Conference on Lightning (APL)*, pp. 547–552. Krabi, Thailand (2017)
14. Liu, Y., et al.: Influence of barrier thickness on discharge behaviour in air gap with GFRP insulator under impulse voltage stress (October). *IEEE Conference on Electrical Insulation and Dielectric Phenomena (CEIDP)*, pp. 971–974. Toronto, Canada (2016)



15. Singh, S., Serdyuk, Y.V.: Simulations of nonthermal electrical discharges in air over solid insulating barrier. *IEEE Trans. Plasma Sci.* 47(1), 729–735 (2018)
16. Tanaka, N., et al.: Difference of discharge phenomena under GFRP and CFRP insulation barrier with steep impulse voltage. In: *IEEE Conference on Electrical Insulation and Dielectric Phenomena (CEIDP)*, pp. 566–569. Cancun, Mexico (2018)
17. Zhelezniak, M.B., Mnatsakanian, A.K., Sizykh, S.V.: Photoionisation of nitrogen and oxygen mixtures by radiation from a gas discharge. *High Temp Sci.* 20(3), 357–362 (1982)
18. Madsen, S.F., et al.: Breakdown tests of glass fibre reinforced polymers (GFRP) as part of improved lightning protection of wind turbine blades.

Conference Record of the 2004 IEEE International Symposium on Electrical Insulation. IEEE, pp. 484–491. Indianapolis (2004)

**How to cite this article:** He, H., et al.: Simulation of positive streamer propagation in an air gap with a GFRP composite barrier. *High Volt.* 6(6), 1079–1091 (2021). <https://doi.org/10.1049/hve2.12112>